Engineering Science and Technology, an International Journal 55 (2024) 101759

Contents lists available at ScienceDirect

Engineering Science and Technology, an International Journal

journal homepage: www.elsevier.com/locate/jestch

Mitigating solidification cracking during the laser welding of extruded Al–Mg–Si alloys by tailoring the microstructure

Jaeheon Lee [a,1,2], Junmyoung Jang [a,1,3], Sangbyuk Lee [a,4], Mungu Kang [b,5], Taeseong Lim [b,6], Seung Hwan Lee [a,7,*]

[a] Department of Mechanical Engineering, Hanyang University, 222 Wangsimni-ro, Seongdong-gu, Seoul, 04763, Republic of Korea
[b] Research & Development Division, Hyundai Motor Group, Hwaseong 18280, Republic of Korea

ARTICLE INFO

Keywords:
Laser welding
Solidification crack
Extruded alloy
Coaxial dual-beam
Surface machining
Microstructural tailoring

ABSTRACT

This study proposes a novel approach for mitigating the internal solidification cracking that occurs during the laser welding of extruded Al–Mg–Si alloys. The microstructures of the extruded alloy, such as the peripheral coarse grains (PCGs) distributed on the surface and the fibrous grain distributed internally, are closely related to these cracks. Therefore, to investigate the effect of the texture of the base metal on internal cracking, an as-extruded alloy with PCGs distributed on the surface and an alloy with the PCGs removed through surface machining were used as the base metal for overlap welding. Furthermore, welding was performed by a coaxial dual-beam laser with four different core-to-ring power ratios to determine the effect of this ratio on the formation of internal cracks. Then, cross-sections of the weld specimens were analysed to compare the cracks, pores, and microstructural texture, such as the grain size, morphology, and grain orientation. Machining away the PCGs on the surface resulted in the formation of columnar grains with low-angle grain boundaries, and it reduced the number of internal cracks that formed along the fusion line. Moreover, dual-beam laser welding followed by surface machining led to the formation of low-angle grain boundaries along the fusion line and grain refinement in the weld centre, thereby mitigating internal solidification cracks by tailoring the microstructure of the base and weld metal.

1. Introduction

With the growing necessity to reduce carbon dioxide emissions and improve fuel efficiency in the automotive manufacturing industry, the use of aluminium alloys is increasing because their strength to weight ratio and corrosion resistance are higher than those of steel [1,2]. Among aluminium alloys, Al–Mg–Si alloys are employed to fabricate various types of parts such as doors and frames by welding and joining after rolling or extrusion [3,4]. As a method of fabricating such parts, laser welding has gained attention owing to its low geometric limitations, low thermal distortion, and high productivity [5,6].

However, during the laser welding of Al–Mg–Si alloys, solidification cracking frequently occurs as the molten pool solidifies, which weakens the weld strength, creep, and fatigue resistance [7,8]. Solidification cracks form during the solidification process of the molten pool when the stress caused by thermal contraction and solidification shrinkage is concentrated at pores and cavities filled with liquid in the semi-solid region and then propagates along the liquid film in the grain boundary [8,9]. The liquid film through which the cracks propagate is formed by the segregation of elements such as Mg, Si, and Fe in the liquid state

* Corresponding author.
E-mail addresses: jaeheonlee@hanyang.ac.kr (J. Lee), jmjang@hanyang.ac.kr (J. Jang), lsb0852@hanyang.ac.kr (S. Lee), mungu.kang@hyundai.com (M. Kang), tslim@hyundai.com (T. Lim), seunghlee@hanyang.ac.kr (S.H. Lee).
[1] These authors contributed equally to this work.
[2] https://orcid.org/0000-0002-7405-3055.
[3] https://orcid.org/0000-0001-9966-0292.
[4] https://orcid.org/0000-0001-9071-2367.
[5] https://orcid.org/0000-0001-7424-3230.
[6] https://orcid.org/0000-0002-7875-211X.
[7] https://orcid.org/0000-0002-1509-3348.

https://doi.org/10.1016/j.jestch.2024.101759
Received 3 April 2024; Received in revised form 5 June 2024; Accepted 30 June 2024
Available online 4 July 2024

at the grain boundary owing to constitutional supercooling during the solidification process [9]. In particular, the columnar grain zone (CGZ), which has coarser grains than the equiaxed grain zone (EGZ), is more susceptible to solidification cracking because the thermal stress is concentrated in a small number of grain boundaries [8,9]. In contrast, the EGZ contains finer grains and has more grain boundaries than the CGZ, which disperses the thermal stress; thus, the EGZ is less susceptible to solidification cracking [10]. As a result, increasing the distribution of equiaxed grains in the weld zone rather than columnar grains is advantageous for mitigating solidification cracking during the laser welding of Al–Mg–Si alloys.

Several grain refinement methods for increasing the distribution of equiaxed grains have been investigated. One strategy for forming equiaxed grains in the weld zone is the use of a high laser power and high welding speed [11–14]. A high laser power can reduce the temperature gradient within the molten pool, and a high welding speed can increase the growth rate, thereby increasing the distribution of equiaxed grains in the centre of the weld zone. Another grain refinement method is the implementation of an ultrasonic vibration device during laser welding, which can increase the distribution of equiaxed grains in the centre of the weld zone by exciting grain nuclei during the solidification of the molten pool [15–17]. Additionally, modulating the laser beam can reduce the temperature gradient of the molten pool, thereby increasing the distribution of equiaxed grains in the centre of the weld zone [18–21]. A coaxial dual-beam laser, a recently developed type of modulated beam, can adjust the distribution of the thermal profile within the molten pool by distributing the laser power output between core and ring beams, which can reduce solidification cracking while ensuring sufficient laser penetration depth in the weld metal [20,21]. All of these methods primarily rely on increasing the distribution of the equiaxed grains in the centre of the weld zone to reduce the solidification cracks propagating along the weld centreline zone during the solidification process. However, solidification cracks, including not only centreline cracks observed on the bead surface but also internal cracks observed in the cross-section of the weld metal, still result in welding quality issues in Al–Mg–Si alloys [22].

Therefore, these internal cracks are closely related to the texture of the base metal [23,24]. Recently, as the electric vehicle industry has become active, extruded Al–Mg–Si alloys have been widely used for frame members and the battery tray of the car body, and internal cracks are a major cause of deteriorating the quality of the weld metal in the laser welding of this material. Sun et al. [25], observed numerous internal cracks at the grain boundaries of columnar grains after laser welding an extruded Al–Mg–Si alloy, and these internal cracks deteriorated the fatigue resistance of the weld metal. Furthermore, in their other study, they proposed a method for reducing solidification cracking during the laser welding of the extruded Al–Mg–Si alloy by modulating the laser beam and adding a filler wire [22]. They reported that controlling the heat input by modulating the laser beam could reduce centreline cracks, while adjusting the chemical composition of the weld metal using filler wire effectively reduced the internal cracks. These studies elucidated the impact of internal cracks on the mechanical properties of a laser-welded extruded alloy and suggested methods for reducing the formation of internal cracks by using laser beam modulation or filler wire. However, research on internal cracks occurring in the laser welding of extruded Al–Mg–Si alloys is still scarce. In particular, the effects of the base metal texture and pores on the formation of internal cracks have not yet been investigated. If the influence of the characteristic microstructure that forms during the manufacturing process of extruded Al–Mg–Si alloys on internal cracks is determined, it could serve as a starting point for developing methods for mitigating internal cracks.

Therefore, this study proposes a novel approach for reducing the amount of solidification cracks by tailoring the microstructure of the base and weld metals during the laser welding of an extruded Al–Mg–Si alloy. In the microstructure of this alloy, randomly oriented peripheral coarse grains (PCGs) are distributed on the surface, while fine, fibrous grains with a uniform orientation are distributed internally [26,27]. To investigate the effect of each of these two types of texture on solidification cracking in the extruded Al–Mg–Si alloy, two base metals were prepared for laser welding: an as-extruded (AE) alloy, in which PCGs were distributed on the surface, and a surface-machined (SM) alloy, in which the PCGs were removed from the surface through surface machining. These two base metals were then overlap welded using a coaxial dual-beam laser, which could mitigate pore formation according to the power ratio of the core and ring beams. To compare the effects of the surface machining of the base metal and the power ratio of the dual-beam laser on solidification cracking, the pores and cracks in cross-sections of the weld zones were quantitatively analysed. In addition, based on an electron backscatter diffraction (EBSD) analysis, the influence of the microstructure on solidification cracking was further investigated by comparing the grain size, grain morphology, and grain orientation under each set of conditions.

2. Experimental procedures

As shown in Fig. 1, a 1.5-mm-thick upper sheet of alloy AA6082-T6 and a 3.5-mm-thick lower sheet were overlap-welded. The dimensions of both sheets were 30 mm × 130 mm, and their chemical composition is listed in Table 1. According to He et al. [28], one-sided constraints significantly induce thermal displacement, making the material more susceptible to solidification cracking; thus, double-sided constraints were applied to the long sides of the base metal [28]. Additionally, Wang et al. [29], reported that the narrower distance between the weld seam and the constraint, the more susceptible it is to solidification cracking; accordingly, this distance was set to 10 mm in this study. Welding was performed from the short side of the base metal along the y-axis direction from +15 mm to +115 mm. The welding process utilized a 4 kW disk laser (Trumpf, Trudisk 4000) with a wavelength of 1030 nm, and the intensity distribution of the laser beam could be adjusted by applying different powers in the core and ring beams. As shown in Fig. 1 (a), the diameters of the core and ring beams at the focus plane were set to 100 and 400 μm, respectively. In addition, a six-axis industrial robot (KUKA, KR22-1610) with a controller (KUKA, KR C4) was coupled to the laser head to control the welding path. To prevent back reflection during welding, the laser head was tilted 10° from the Z-axis. The process parameters for welding process of this study are listed in Table 2.

Fig. 1(b) shows cross-sectional optical micrographs of the AE and SM base metals, which were used to investigate the effect of the texture of the alloy on solidification cracking. In the cross-section of the AE base metal, a PCG layer approximately 0.5 mm thick appears on the surfaces of both the upper and lower sheets, with a fine fibrous grain texture between the PCG layers. This distinct texture was formed during the hot extrusion of the Al–Mg–Si alloy, wherein abnormal recrystallization occurs on the material surface owing to the heat input into the materials and the friction between the die and the material, thus forming PCGs with coarse, randomly oriented grains [27,30]. Additionally, the uncrystallized region within the material elongated in the direction of metal flow, forming fibrous grains with a fine grain size and uniform orientation, thus exhibiting strong texture [27,31]. For the SM base metal, the surface was machined away to remove the PCGs from the AE base metal, leaving only the fibrous grains. To ensure that the SM and AE specimens had the same thickness, the extruded alloy sheet that was used to prepare the SM specimens was 2 mm thicker than that used for the AE specimens; thus, after machining away 1 mm from each side, the SM specimens were of the same thickness as the AE ones.

As listed in Table 3, with the total power of the laser fixed at 3 kW, the core/ring beam power ratio was set to 100:0, 70:30, 50:50, or 30:70, and all other process variables were kept the same, as shown in Table 2. To ensure the reproducibility of the results, three experiments were performed for each set of conditions. As shown in Fig. 1(c), the welded specimen was cut at sections A–A' and B–B' and etched with a 1 % NaOH

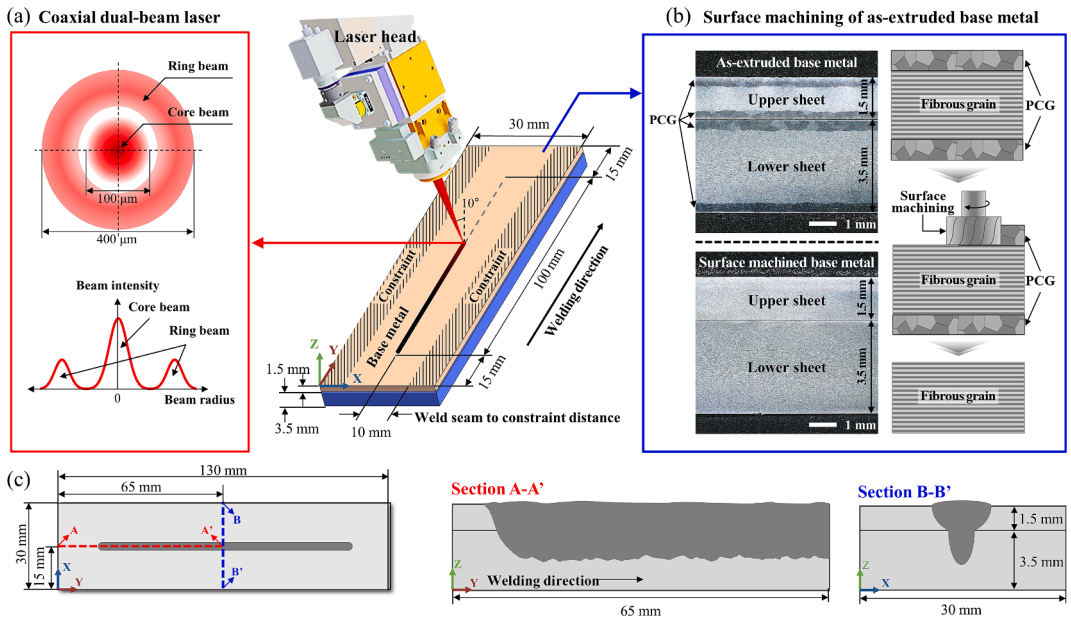

Fig. 1. Experimental setup: (a) schematic diagram of the experimental system used for the laser welding of extruded Al–Mg–Si alloy, (b) cross-sections and preparation process of the AE and SM specimens, and (c) position of the cross-sectional analysis of the welds.

Table 1
Chemical composition (wt%) of the base metal.

	Al	Mg	Si	Mn	Fe	Cr	Cu	Ti	Zn	others
AA6082-T6	97.35	0.96	0.93	0.54	0.11	0.02	0.02	0.01	0.01	0.05

Table 2
Laser welding process parameters.

Laser power (W)	3000
Wavelength (nm)	1030
Beam diameter (mm)	Core beam: 0.1; Ring beam: 0.4;
Welding speed (m/min)	4
Laser head tilt angle (degree)	10
Focal position (mm)	+0 (base metal surface)

Table 3
Experimental conditions.

Base metal condition	Power ratio (Core/Ring)	Core beam power (W)	Ring beam power (W)
As–extruded (AE)	100:0	3000	0
	70:30	2100	900
	50:50	1500	1500
	30:70	900	2100
Surface machined (SM)	100:0	3000	0
	70:30	2100	900
	50:50	1500	1500
	30:70	900	2100

solution. An optical microscope (Olympus, DSX 110) was used to examine the pores and cracks in the cross-section obtained from section A–A'. In addition, field-emission scanning electron microscopy (FE-SEM; Thermo Scientific, Quattro S) was used to analyse the fractography of the observed cracks. Moreover, EBSD (EDAX-AMETEK Inc., Velocity Super) was used to analyse the morphology, size, and orientation of the grains in the cross-sections of the welded specimens obtained from sections A–A' and B–B'.

3. Results and discussion

3.1. Solidification cracking in laser welds of the extruded Al–Mg–Si alloy

Fig. 2 shows optical micrographs of longitudinal cross-sections of AE specimens under four different power ratios of core and ring beams. The dashed line indicates the joint interface, while the dotted line indicates the fusion line. As shown in Fig. 2(a–d), numerous cracks formed near the joint interface under all conditions. To observe these cracks near the joint interface in more detail, the areas within the dashed box for each condition were magnified, as shown in Fig. 2(e–h). Porous cracks, in which both pores and cracks appeared, and non-porous cracks, which had no pores, were both observed in the weld zone of all AE specimens. In addition, regardless of the type of crack, all cracks propagated in the z-direction toward the top of the weld bead. Comparing the pores among the four power ratios, the highest number of pores was observed when only the core beam laser was used (i.e., core/ring = 100:0). Furthermore, among the dual-beam conditions, the core/ring = 70:30 ratio resulted in the fewest pores. Meanwhile, the pore size increased with the increasing power of the ring beam. In particular, when the power of the ring beam was greater than that of the core beam (core/ring = 30:70), not only did the pore size become the largest, but also, humping occurred at the bead surface, as shown in Fig. 2(d).

Fig. 3 shows the longitudinal cross-section of the weld zone in the SM specimens under four different core/ring power ratios. Similar to the AE specimens, the cracks were primarily distributed near the joint interface, as indicated by the arrows. In the magnified images of the dashed box shown in Fig. 3(e–h), porous cracks appear for all SM conditions, similar to those seen in the AE specimens. However, unlike the non-porous cracks observed in all AE specimens, non-porous cracks are scarcely visible to the naked eye in the SM specimens. This indicates that the presence of PCGs distributed on the surface of the extruded alloy is related to the formation of non-porous cracks. In addition, the formation

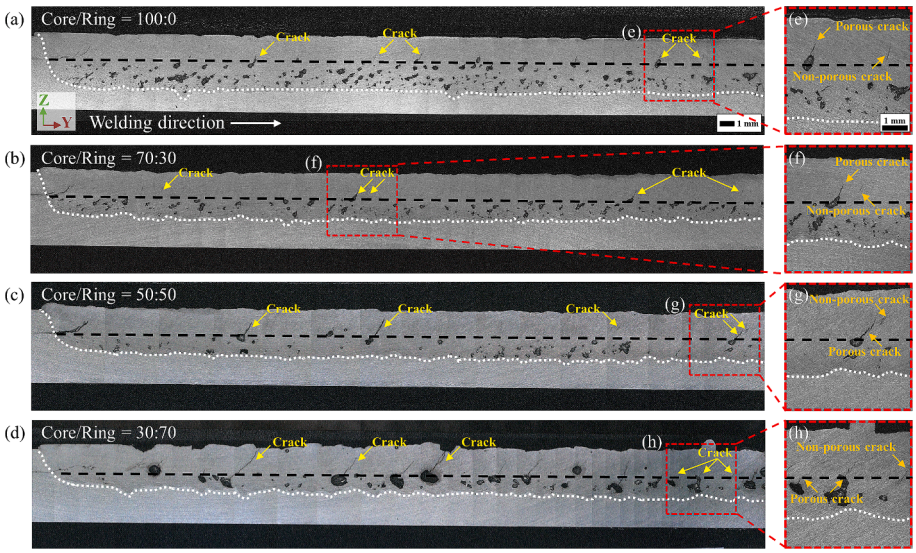

Fig. 2. Longitudinal cross-sections of the weld zone in the AE specimens according to the core/ring power ratio: (a) 100:0, (b) 70:30, (c) 50:50, and (d) 30:70, and (e–h) corresponding magnified images from the dashed boxes.

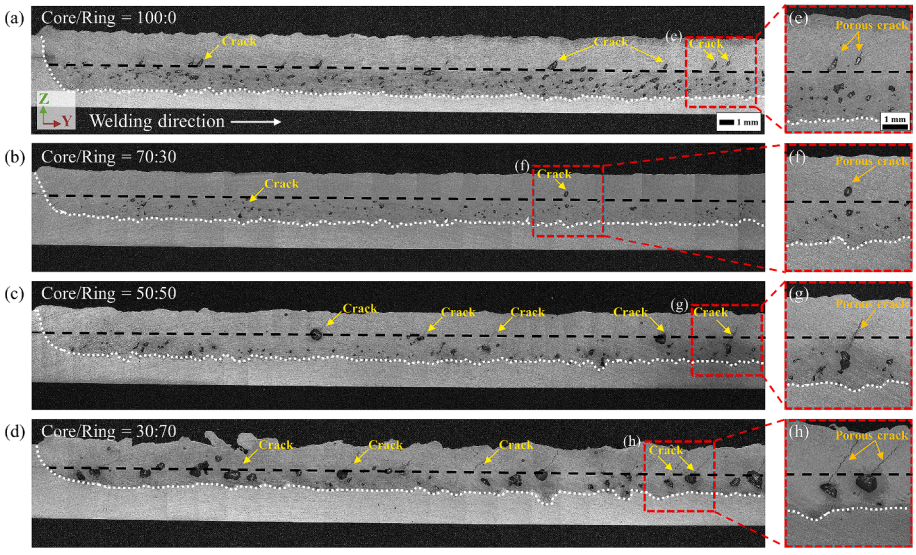

Fig. 3. Longitudinal cross-section of the weld zone in SM specimens according to the core/ring power ratio: (a) 100:0, (b) 70:30, (c) = 50:50, (d) 30:70, and (e–h) corresponding magnified images from the dashed boxes.

of pores under the four different core/ring power ratios showed a similar trend in both AE and SM specimens, as shown in Fig. 3(a–d).

To verify whether the porous and non-porous cracks are both solidification cracks, SEM–EDS analysis was performed on the cracks observed in the longitudinal cross-section of the AE specimen. Fig. 4(a) shows an SEM image of a porous crack, which is a crack propagating from a pore, while Fig. 4(d) shows a non-porous crack formed in an area without pores. These two types of cracks have different formation mechanisms. Porous cracks occur when the liquid film along the grain boundary tears due to thermal stress concentrated on the pores formed during the solidification process of the molten pool [9,32]. In compared, non-porous cracks occur when the liquid film along the grain boundary tears because of thermal stress concentrated on cavities filled with liquid instead of empty pores [9,32]. To further investigate the morphology of the fracture surfaces of each crack, the dashed box areas were magnified, revealing that both cracks exhibited a smooth dendritic fracture surface. This type of surface is known to indicate the solidification of a liquid film, which is ruptured by a solidification crack [33]. To determine whether the dendritic fracture surface observed on the fracture surfaces of each crack was formed by a liquid film, EDS line scanning was performed to analyse the composition analysis along the lines indicated in Fig. 4(a, d). The liquid film formed during the welding process of Al–Mg–Si alloys was primarily composed of eutectic liquids such as Mg–Si and Al–Fe–Si. Because Mg has a low boiling point (1091 °C), leading to a high vaporization during the laser welding, the compositions of remaining Si and Fe were investigated. As shown in Fig. 4(b), the line scan results from an area without porous cracks indicated Si and Fe compositions of approximately 1.04 and 0.27 wt%, respectively, which are close to the chemical composition of the base metal listed in Table 1. In contrast, the line scan across the porous crack showed Si and Fe contents as high as 23 and 4 wt%, respectively, near the porous crack region, as illustrated in Fig. 4(c). Similarly, as shown in Fig. 4(e), the line scan of line e indicated Si and Fe compositions with those in line b. However, the line scan across the non-porous crack, represented by line f, showed increases in the Si and Fe compositions to as much as 23 and 8 wt%, respectively, as depicted in Fig. 4(f). This indicates the segregation

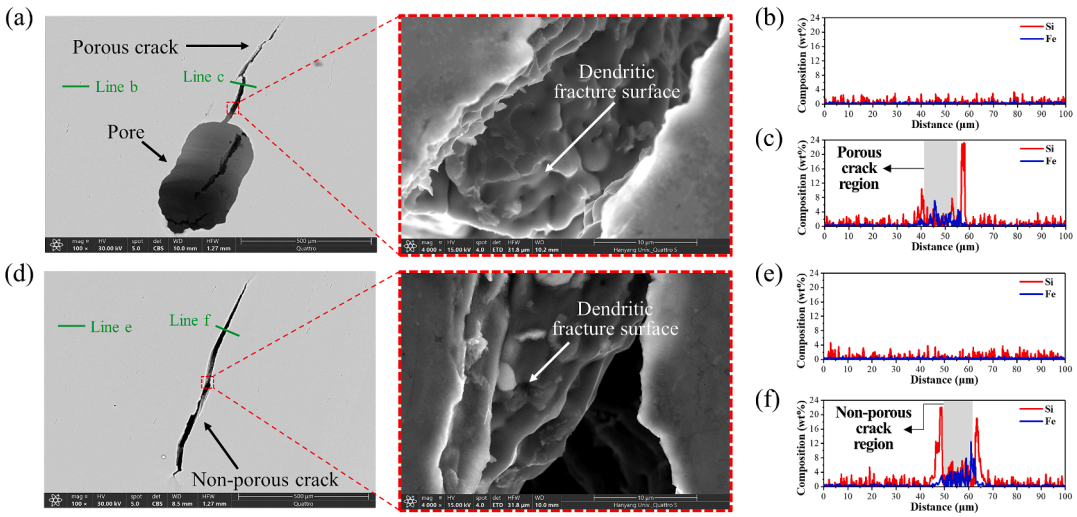

Fig. 4. Magnified images of the cracks observed in the longitudinal cross–section view of the weld zone in AE specimen applying core beam laser (Core/Ring = 100:0): (a) porous crack, (b) none–porous crack.

of Si and Fe along the propagation paths of both the porous and non-porous cracks. This segregation identified in porous cracks and non-porous cracks demonstrated that both types of cracks are solidification cracks formed by tearing of the liquid film. Among the constituent elements of the Al–Mg–Si alloy, Si and Fe have relatively lower solubility and diffusivity in the Al matrix than the other elements [34,35]. Therefore, as the dendrites grow at the solid–liquid interface of the molten pool, Si and Fe are constantly rejected into the liquid [36,37]. Consequently, the residual liquid enriched with Si and Fe has a lower solidification temperature owing to the constitutional supercooling effect, thereby delaying solidification compared to that of Al [38]. As a result, during the final stages of solidification (solid fraction >0.9), the eutectic liquid enriched with Si and Fe remains at the grain boundaries, forming a liquid film. In summary, the dendritic fracture surface and the segregation of Si and Fe near the cracks confirm that the porous and non-porous cracks observed in Figs. 2 and 3 are both internal solidification cracks formed during the solidification of the molten pool.

To quantitatively compare the influence of the dual-beam laser and surface machining on the formation of the internal cracks, the number of cracks and the area fraction of pores were measured in magnified longitudinal cross-sectional views of each specimen. Fig. 5 shows the measured number of cracks and the area fraction of pores observed under each condition in the weld zones of AE and SM specimens. In the bar graphs, the numbers of porous and non-porous cracks are represented as blue and orange, respectively, with the total number of solidification cracks being the sum of both types of cracks. The area fraction of pores, shown as a black line, represents the ratio of the total area of pores to the total area of the weld zone. To ensure the reproducibility of the results, the area fraction of pores and the numbers of both types of cracks were averaged from three cross-sections obtained under each condition. As shown in Fig. 5(a), the number of porous cracks in the AE specimens welded under core/ring power ratios of 70:30 and 50:50 was 73 % and 27 % lower, respectively, than that in the specimen welded using only core beam laser (100:0). Conversely, more porous cracks appeared with a power ratio of 30:70 (i.e., a higher ring beam power). To understand this trend in the occurrence of porous cracks, the area fraction of pores, which initiate porous cracks, was analysed for each condition. The results showed that, similar to the trend in the porous crack occurrence, the pore area fraction was lowest under the core/ring power ratio of 70:30, and the area fraction of pores increased with increasing ring beam power. This reduction in pores when using a dual-beam laser is due to changes in the behaviour of the molten pool and keyhole depending on the core/ring power ratio. According to Li et al. [39], when the power of the core beam is greater than that of the ring beam, the ring beam helps to alleviate the temperature gradient on the surface of the molten pool, stabilizing the melt flow and thus reducing the collapse of the keyhole. However, when the power of the ring beam is greater than that of the core beam, the decreased power density leads to a lower recoil pressure for keyhole formation, resulting in an unstable molten pool and the formation of larger pores [40]. On the other hand, the non-porous cracks observed in the AE specimens welded under the dual-beam laser at all ratios decreased with respect to those welded using only the core beam laser (core/ring = 100:0). Among the three dual-beam conditions, the condition with a power ratio of 30:70 showed the fewest non-porous cracks, but the higher power of the ring beam led to the excessive formation of pores in the unstable molten pool, increasing the number of porous cracks with respect to that with only the core beam laser. In comparison, the power ratio of 70:30 resulted in a significant reduction in both porous and non-porous cracks with 100:0 (core beam only), resulting in the fewest total number of cracks. The influence of the power ratio on non-porous cracks is due to changes in the temperature gradient of the molten pool caused by the

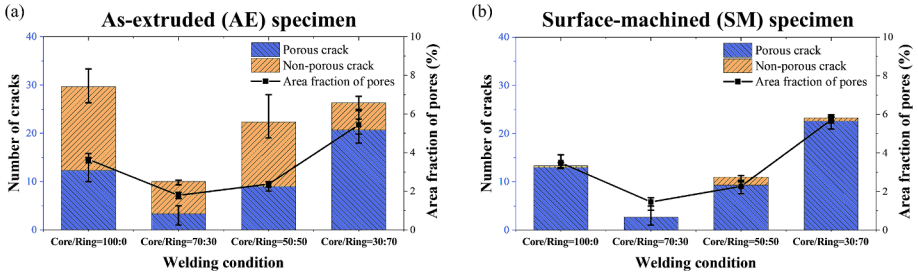

Fig. 5. Number of cracks and area fraction of pores measured in the longitudinal section of the weld zone according to the base metal: (a) AE and (b) SM.

ring beam, which alters the microstructure of the weld associated with crack propagation. The effect of the microstructural differences in the welds caused by the coaxial dual-beam on the formation of internal solidification cracks is discussed in Section 3.2.

Fig. 5(b) shows the measured number of cracks and the area fraction of pores in the weld zone of the SM specimens, where the PCGs on the surface of the extruded alloy were removed. The number of porous cracks and the area fraction of pores, which act as initiators for these cracks, were lowest under the condition with a core/ring power ratio of 70:30 among the four power ratio conditions. Additionally, when using a coaxial dual-beam, increasing the ring beam power increased both the number of porous cracks and the area fraction of pores. In other words, the porous cracks observed in the SM and AE specimens exhibited similar trends depending on the core/ring power ratio. Unlike the results for porous cracks, all SM specimens exhibited significantly fewer non-porous cracks than the AE specimens. This indicates that the difference in the microstructure of the welds due to the removal of PCGs from the extruded material during surface machining is associated with the reduction of non-porous cracks. The effect of these microstructural differences in the base metal caused by surface machining on the formation of internal solidification cracks is discussed in Section 3.3. To sum up the results of both AE and SM specimens, the total number of cracks in the SM specimen using the core/ring power ratio of 70:30 was approximately 91 % lower than that in the AE specimen using the core beam (100:0), representing the most significant reduction in solidification cracks. This indicates that the application of both surface machining and a dual beam (core/ring = 70:30) during the laser welding process of extruded Al–Mg–Si alloy provides the most effective reduction in solidification cracks. Additionally, as shown in Supplementary Fig. S1, comparing the average lengths of the cracks between the AE and SM specimens did not show a significant difference.

3.2. Effect of the coaxial dual-beam laser on solidification cracking

To investigate the reason for the reduction in internal cracks when using the dual-beam laser compared to the core beam laser, EBSD analysis was performed on the cross-sectional microstructure of the weld zone, as shown in Fig. 6. For the EBSD analysis, the conditions selected for both the AE and SM specimens were the core/ring power ratio of 70:30, which showed the most significant reduction in solidification cracks, and the core beam only (i.e., core/ring = 100:0). As shown in the inverse pole figure (IPF) map images of the longitudinal section of the weld zones in Fig. 6(a–d), equiaxed grains are commonly distributed in the upper and lower regions under all conditions, while columnar grains grown in the YZ direction are distributed between the two equiaxed grain regions. The magnified images of the CGZ for each condition in Fig. 6(e–h) reveal that internal cracks propagate along the columnar grain boundaries in the YZ direction. The propagation direction of these cracks matches the propagation direction of the porous and non-porous cracks observed in Fig. 2 and Fig. 3. To examine the differences in the distribution of columnar grains where internal cracks occur depending on the type of laser, the grain shape aspect ratio (GSAR), which distinguishes columnar grains from equiaxed grains, was analysed. GSAR is the ratio of the major axis to the minor axis of the ellipse inscribed around a grain, and grains with a GSAR of 0.33 or less can be classified as columnar grains [41]. The colour map images in Fig. 6(i–l) show the GSAR divided into five levels, with the areas enclosed by dotted lines representing the CGZ, and the remaining areas representing the EGZ. As shown in Fig. 6(i, k), when only the core beam laser was applied, the CGZ and EGZ were mixed at the joint interface, as indicated by the dashed line. In contrast, when the dual beam was applied (Fig. 6(j, l)), equiaxed grains formed at the joint interface. This indicates that the dual beam reduces the distribution of columnar grains and increases the distribution of equiaxed grains at the centre of the weld.

To quantitatively confirm the distribution of columnar grains and equiaxed grains at the joint interface depending on the type of laser, the size and morphology of the grains were measured, as shown in Fig. 7. Fig. 7(a–d) shows the average grain size measured at the joint interface under each condition, and Fig. 7(e–h) shows the distribution of CGZ and EGZ at the joint interface based on the GSAR. Comparing the measurements for the AE specimens under the conditions using the core beam laser and the dual-beam laser, the dual beam decreased the average grain size at the joint interface from 136.795 to 66.702 μm and increased the fraction of EGZ from 54.31 % to 89.55 %, as shown in Fig. 7(a, b, e, f). Similarly, in the SM specimen, comparing the conditions using the core beam laser and the dual-beam laser, the dual beam decreased the

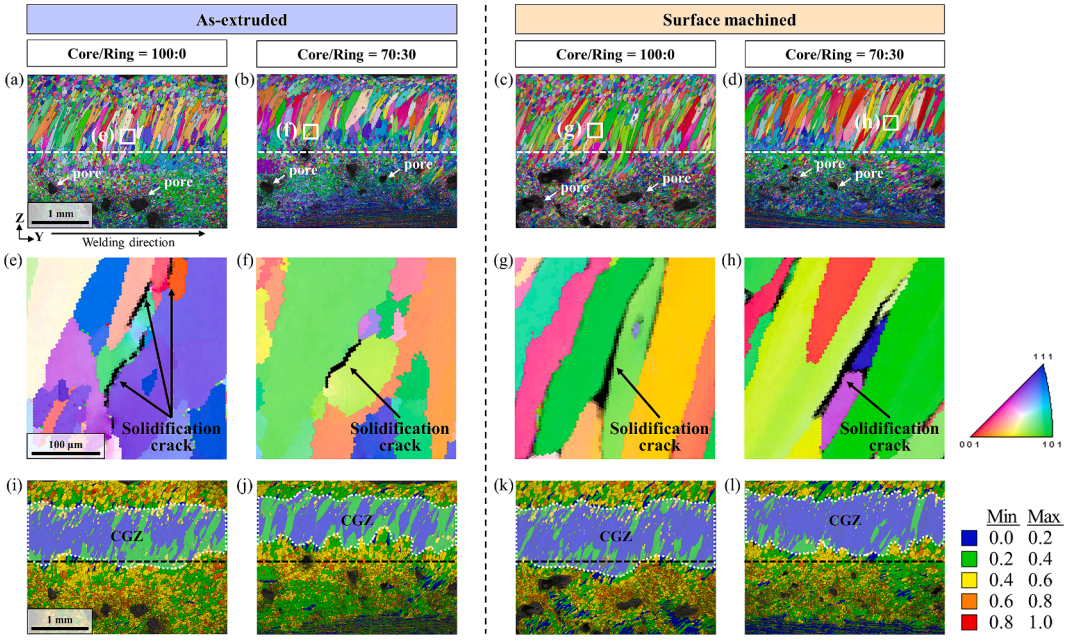

Fig. 6. EBSD results of longitudinal sections for (left to right) the AE specimen with the core beam laser (100:0), the AE specimen with the dual-beam laser (70:30), the SM specimen with the core beam laser (100:0), and the SM specimen with the dual-beam laser (70:30): (a–d) IPF maps, (e–h) enlarged images of solidification cracks in the IPF maps, and (i–l) GSAR maps.

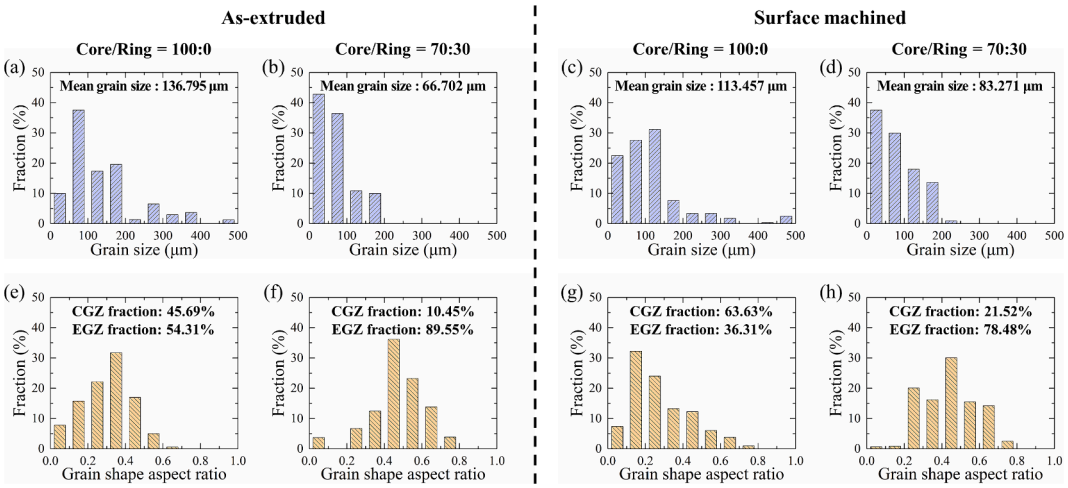

Fig. 7. Joint interface analysis for the AE specimen with the core beam laser (100:0), the AE specimen with the dual-beam laser (70:30), the SM specimen with the core beam laser (100:0), and the SM specimen with the dual-beam laser (70:30): (a–d) grain size analysis of the joint interface and (e–h) grain morphology analysis according to the fraction of each GSAR at the joint interface.

average grain size at the joint interface and increased the fraction of EGZ, as shown in Fig. 7(c, d, g, h). This indicates that the dual-beam laser (core/ring = 70:30) resulted in grain refinement by increasing the distribution of fine equiaxed grains at the weld centre in both AE and SM specimens.

The differences in grain size and grain morphology resulting from the use of the dual-beam laser are attributed to the ring beam surrounding the core beam during welding. When using only the core beam, which has a conventional Gaussian energy distribution, a significant energy difference occurs between the centre and the edges of the laser-irradiated area. In contrast, the dual-beam laser, consisting of a core beam and a surrounding ring beam, decreases the energy difference between the centre and edges of the irradiated area owing to the heat input from the ring beam. This smaller difference in the energy distribution caused by the ring beam in turn mitigates the temperature gradient within the molten pool formed during the laser welding process [42]. According to Kou et al. [43], the grain size can be expressed as the product of the temperature gradient (G) and the growth rate (R), and lower G/R values result in a grain morphology of equiaxed grains. Therefore, when welding with a dual-beam laser, the decrease in G within the molten pool leads to grain refinement, increasing the fraction of equiaxed grains. This grain refinement increases the number of grain boundaries per unit area. In particular, if the grains near the joint interface, where thermal stress is concentrated, become finer, this stress is dispersed, suppressing the propagation of solidification cracks. Hence, the reduction in non-porous cracks observed in the longitudinal section of both AE and SM specimens when using a dual-beam laser (core/ring = 70:30), as shown in Fig. 5, can be attributed to the grain refinement resulting from the lower temperature gradient occurring under the dual-beam laser compared to that under only the core beam.

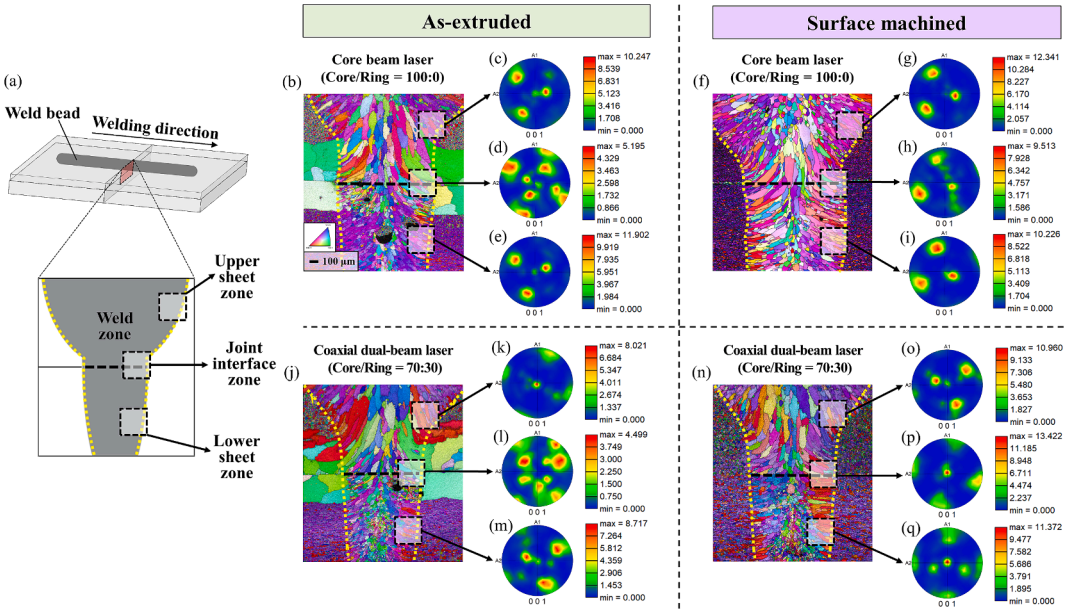

Fig. 8. EBSD results from the transverse cross-sections: (a) schematic of the IPF map of the transverse cross-section, (b) IPF map of the AE specimen with the core beam laser (100:0) and (c–e) [001] contoured pole figures (upper sheet, joint interface, lower sheet), (f) IPF map of the SM specimen with the core beam laser (100:0) and (g–i) [001] contoured pole figures (upper sheet, joint interface, lower sheet), (j) IPF map of the AE specimen with the dual-beam laser (70:30) and (k–m) [001] contoured pole figures (upper sheet, joint interface, lower sheet), (n) IPF map of the SM specimen with the dual-beam laser (70:30) and (o–q) [001] contoured pole figures (upper sheet, joint interface, lower sheet).

3.3. Effect of surface machining on the solidification cracking

To investigate why internal solidification cracking occurs less frequently in SM specimens, where PCGs are removed through surface machining, than in AE specimens, where the PCGs are distributed on the surface of extruded materials, EBSD analysis was performed on transverse cross-sections of both the AE and SM specimens. Fig. 8(a) schematically illustrates the weld observed in the transverse cross-section. The dotted and dashed lines represent the fusion line and joint interface, respectively. Within the weld zone, the three regions (the upper sheet zone, the joint interface zone, and the lower sheet zone) denote the specific areas analysed for microstructural variations in the weld region, influenced by the textures of AE and SM specimens. As shown in Fig. 8(b, j), PCGs are distributed in the base metal region near the joint interface in AE specimens. In contrast, in SM specimens, the PCGs have been removed; thus, the base metal region is composed entirely of fine grains, as shown in Fig. 8(f, n). As shown in the pole figures of Fig. 8(c, e), in the AE specimens welded using a core beam laser, the grains in the upper and lower sheets grow from the fusion line with relatively uniform crystal orientations. In contrast, near the fusion line in the joint interface, a variety of grain orientations are observed, as shown in Fig. 8(d). Furthermore, the multiples of uniform distribution (MUD) value, which indicates the strength of the grain orientation, is lower around the joint interface than those in the upper and lower sheets. As shown in the pole figures of Fig. 8(g-i), in the conditions where the core beam laser was applied to the SM specimens with PCG removed through surface machining, it can be observed that grains with relatively uniform crystallographic orientation grow not only in the upper and lower sheet zones but also in the joint interface zone from the fusion line. When comparing the MUD values in these three zones of the SM specimens welded using the core beam laser, a high intensity of over 9.5 was observed in all three zones. Moreover, this difference of grain orientation in the weld zones of the AE specimens and the SM specimens, when welded using the core beam laser, was also found in the specimens welded using the coaxial dual-beam laser, as shown in Fig. 8(k-m) and Fig. 8(o-q). The reason for this texture difference in the weld zones of AE and SM specimens is that the orientation of the columnar grains growing from the fusion line is influenced by the texture of the base metal. In AE specimens, where PCGs are distributed on the surface, fibrous grains with a relatively uniform orientation form inside the upper and lower regions of the sheets owing to metal flow during the extrusion process. However, on the surface of the material, PCGs with random crystal orientations form because of abnormal recrystallization. As a result, in the upper and lower sheet portions of the weld zone, grains with relatively uniform texture grow along the fusion line from the fibrous grains, whereas near the joint interface, where PCGs are heavily distributed, coarse columnar grains with diverse orientations grow epitaxially along the fusion line. In the SM specimens, the removal of the PCGs, which cause the growth of columnar grains with diverse orientations, results in a fibrous grain texture in all regions of the base metal, leading to a highly oriented texture in the columnar grains across all three regions.

To investigate the impact of the difference in grain texture between the AE and SM specimens on the reduction of internal solidification cracks, the misorientation angle (θ) of columnar grains growing along the fusion line in the joint interface region was measured in each specimen. As shown in Fig. 9(a), in the joint interface region of AE specimens welded using the core beam only, which exhibited various grain orientations, the fraction of high-angle grain boundaries (HAGBs, $\theta > 15°$) was larger than that of low-angle grain boundaries (LAGBs, $\theta \leq 15°$). In contrast, as shown in Fig. 9(b), near the joint interface in SM specimens welded with the core beam laser, which exhibited relatively uniform grain orientation, the fraction of LAGBs was larger than that of HAGBs. This difference in grain boundaries was also observed in the dual-beam specimens, as shown in Fig. 9(c, d). To sum up, columnar grains with various orientations predominantly contained HAGBs, whereas a more uniform grain orientation increased the distribution of LAGBs. According to Ma et al. [44], columnar grains with HAGBs are more susceptible to solidification cracking than columnar grains with LAGBs because a liquid film forms more easily at these grain boundaries. Therefore, reducing the distribution of HAGBs and increasing the distribution of LAGBs in the CGZ can decrease the susceptibility to solidification cracking. Consequently, the fewer occurrences of non-porous cracks in SM specimens than in AE specimens was attributed to the decreased fraction of HAGBs in the CGZ, where internal cracks primarily form. This result confirmed that removing the PCG, which is the characteristic texture of extruded Al–Mg–Si alloys, through machining away the surface before the laser welding process suppresses the formation of HAGBs, thereby reducing internal solidification cracks.

4. Conclusion

This study proposed a novel strategy for mitigating the internal solidification cracking that occurs during the laser welding of extruded Al–Mg–Si alloys by tailoring the microstructure of base and weld metal. The key findings of this study are as follows.

1. In the laser welding of as-extruded Al–Mg–Si alloy, columnar grains with HAGBs grew epitaxially from the PCGs distributed on the surface of the base metal. In contrast, in the laser welding of surface-machined Al–Mg–Si alloys, columnar grains with LAGBs, which have lower susceptibility to solidification cracking, grew epitaxially along the fusion line of the weld metal
2. Using a coaxial dual-beam laser with a core/ring power ratio of 70:30 resulted in the formation of the fewest pores and increased the amount of equiaxed grains at the joint interface compared with using a conventional core beam laser. Accordingly, porous cracks, which are initiated from pores, and non-porous cracks, which mainly form in the CGZ, were both mitigated
3. The proposed method, which removes the PCGs formed on the surface of as-extruded alloys and then uses a dual-beam laser with a core/ring power ratio of 70:30, can simultaneously refine grains and suppress the formation of HAGBs. Consequently, this combined strategy mitigated the amount of internal solidification cracks by approximately 91 % with respect to that in as-extruded alloys welded using the core beam

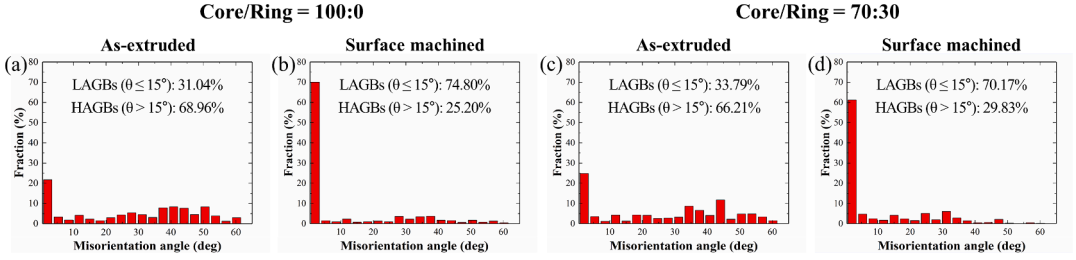

Fig. 9. Grain misorientation angle in the joint interface region near the fusion line: (a) AE specimen with the core beam laser (100:0), (b) SM specimen with the core beam laser (100:0), (c) AE specimen with the dual-beam laser (70:30), (d) SM specimen with the dual-beam laser (70:30).

CRediT authorship contribution statement

Jaeheon Lee: Writing – original draft, Visualization, Methodology, Investigation, Data curation. **Junmyoung Jang:** Writing – review & editing, Visualization, Methodology, Investigation. **Sangbyuk Lee:** Visualization, Software, Data curation. **Mungu Kang:** Resources, Formal analysis. **Taeseong Lim:** Resources, Formal analysis. **Seung Hwan Lee:** Writing – review & editing, Supervision, Project administration, Funding acquisition, Conceptualization.

Declaration of competing interest

The authors declare that they have no known competing financial interests or personal relationships that could have appeared to influence the work reported in this paper.

Acknowledgements

This work was supported by the National Research Foundation of Korea(NRF) grant funded by the Korean government (MSIT) (No. NRF-2023R1A2C1004272).

Appendix A. Supplementary data

Supplementary data to this article can be found online at https://doi.org/10.1016/j.jestch.2024.101759.

References

[1] R. Lu, S. Zheng, J. Teng, J. Hu, D. Fu, J. Chen, G. Zhao, F. Jiang, H. Zhang, Microstructure, mechanical properties and deformation characteristics of Al-Mg-Si alloys processed by a continuous expansion extrusion approach, J. Mater. Sci. Technol. 80 (2021) 150–162.
[2] X. Kai, C. Chen, X. Sun, C. Wang, Y. Zhao, Hot deformation behavior and optimization of processing parameters of a typical high-strength Al–Mg–Si alloy, Mater. Des. 90 (2016) 1151–1158.
[3] N. Hashimoto, Application of Aluminum extrusions to automotive parts, Kobelco Technol. Rev. 35 (2017) 69–75.
[4] J. Hirsch, Recent development in aluminium for automotive applications, Trans. Nonferrous Met. Soc. China. 24 (2014) 1995–2002.
[5] X. Cao, W. Wallace, C. Poon, J.-P. Immarigeon, Research and progress in laser welding of wrought aluminum alloys. I. Laser welding processes, Mater. Manuf. Process. 18 (2003) 1–22.
[6] S.H. Lee, J. Mazumder, J. Park, S. Kim, Ranked feature-based laser material processing monitoring and defect diagnosis using k-NN and SVM, J. Manuf. Process. 55 (2020) 307–316.
[7] O.O. Oladimeji, E. Taban, Trend and innovations in laser beam welding of wrought aluminum alloys, Weld. World. 60 (2016) 415–457.
[8] M. Norouzian, M. A. Elahi, P. Plapper, A review: Suppression of the solidification cracks in the laser welding process by controlling the grain structure and chemical compositions. J. Adv. Join. Process (2023). 100139.
[9] C. Cross, On the origin of weld solidification cracking, Journal. (2005) 3–18.
[10] C. Hagenlocher, D. Weller, R. Weber, T. Graf, Reduction of the hot cracking susceptibility of laser beam welds in AlMgSi alloys by increasing the number of grain boundaries, Sci. Technol. Weld. Join. 24 (2019) 313–319.
[11] C. Böhm, C. Hagenlocher, J. Wagner, T. Graf, S. Weihe, Analytical description of the criterion for the columnar-to-equiaxed transition during laser beam welding of aluminum alloys, Metall. Mater. Trans. A 52 (2021) 2720–2731.
[12] Q. Chu, R. Bai, H. Jian, Z. Lei, N. Hu, C. Yan, Microstructure, texture and mechanical properties of 6061 aluminum laser beam welded joints, Mater. Charact. 137 (2018) 269–276.
[13] C. Hagenlocher, F. Fetzer, D. Weller, R. Weber, T. Graf, Explicit analytical expressions for the influence of welding parameters on the grain structure of laser beam welds in aluminium alloys, Mater. Des. 174 (2019) 107791.
[14] X. Wang, F. Lu, H.-P. Wang, Z. Qu, L. Xia, Micro-scale model based study of solidification cracking formation mechanism in Al fiber laser welds, J. Mater. Process. Technol. 231 (2016) 18–26.
[15] T. Radel, P. Woizeschke, Reduction of hot cracking susceptibility during laser welding of aluminum by vibrations, Weld. World. 63 (2019) 599–606.
[16] A. Teyeb, J. Silva, J. Kanfoud, P. Carr, T.-H. Gan, W. Balachandran, Improvements in the microstructure and mechanical properties of aluminium alloys using ultrasonic-assisted laser welding, Metals 12 (2022) 1041.
[17] T. Radel, Mechanical manipulation of solidification during laser beam welding of aluminum, Weld. World 62 (2018) 29–38.
[18] M. Kang, H.N. Han, C. Kim, Microstructure and solidification crack susceptibility of Al 6014 molten alloy subjected to a spatially oscillated laser beam, Materials 11 (2018) 648.
[19] M. Kang, J. Cheon, D.H. Kam, C. Kim, The hot cracking susceptibility subjected the laser beam oscillation welding on 6XXX aluminum alloy with a partial penetration joint, J. Laser Appl. 33 (2021).
[20] V.V. Pamarthi, T. Sun, A. Das, P. Franciosa, Strain-based investigation on solidification crack susceptibility of 6005 aluminium using adjustable ring mode (ARM) laser welding, Procedia CIRP 111 (2022) 425–430.
[21] V.V. Pamarthi, T. Sun, A. Das, P. Franciosa, Tailoring the weld microstructure to prevent solidification cracking in remote laser welding of AA6005 aluminium alloys using adjustable ringmode beam, J. Mater. Res. Technol. 25 (2023) 7154–7168.
[22] T. Sun, P. Franciosa, M. Sokolov, D. Ceglarek, Challenges and opportunities in laser welding of 6xxx high strength aluminium extrusions in automotive battery tray construction, Procedia CIRP. 94 (2020) 565–570.
[23] L. Aucott, D. Huang, H. Dong, S. Wen, J. Marsden, A. Rack, A. Cocks, Initiation and growth kinetics of solidification cracking during welding of steel, Sci. Rep. 7 (2017) 40255.
[24] S. Tokita, K. Kadoi, Y. Kanno, H. Inoue, Microstructural evolution and solidification cracking susceptibility of grain boundary engineered fully austenitic stainless steel, Weld. World. 64 (2020) 593–600.
[25] T. Sun, P. Franciosa, C. Liu, F. Pierro, D. Ceglarek, Effect of micro solidification crack on mechanical performance of remote laser welded AA6063-T6 fillet lap joint in automotive battery tray construction, Appl. Sci. 11 (2021) 4522.
[26] W.H. Van Geertruyden, H.M. Browne, W.Z. Misiolek, P.T. Wang, Evolution of surface recrystallization during indirect extrusion of 6xxx aluminum alloys, Metall. Mater. Trans. A 36 (2005) 1049–1056.
[27] H. Zhao, L. Sun, G. Zhao, J. Yu, F. Liu, X. Sun, Z. Lv, S. Cao, Abnormal grain growth behavior and mechanism of 6005A aluminum alloy extrusion profile, J. Mater. Sci. Technol. 157 (2023) 42–59.
[28] Q. He, H. Wei, J.-S. Chen, H.-P. Wang, B.E. Carlson, Analysis of hot cracking during lap joint laser welding processes using the melting state-based thermomechanical modeling approach, Int. J. Adv. Manuf. Technol. 94 (2018) 4373–4386.
[29] X. Wang, F. Lu, H.-P. Wang, H. Cui, X. Tang, Y. Wu, Mechanical constraint intensity effects on solidification cracking during laser welding of aluminum alloys, J. Mater. Process. Technol. 218 (2015) 62–70.
[30] P. Goik, A. Schiffl, H. Höppel, Formation of peripheral coarse grain in thin-walled Al–Mg–Si extrusion profiles, Metall. Mater. Trans. A. 54 (2023) 3940–3956.
[31] M. Negozio, R. Pelaccia, L. Donati, B. Reggiani, Numerical investigation of the surface recrystallization during the extrusion of a AA6082 aluminum alloy under different process conditions, Int. J. Adv. Manuf. Technol. 129 (2023) 1585–1599.
[32] T. Böllinghaus, H. Herold, C.E. Cross, J.C. Lippold, Hot Cracking Phenomena in Welds II, Springer Science & Business Media, 2008.
[33] J.C. Lippold, Welding Metallurgy and Weldability, John Wiley & Sons, 2014.
[34] A. Gorny, J. Manickaraj, Z. Cai, S. Shankar, Evolution of Fe based intermetallic phases in Al–Si hypoeutectic casting alloys: Influence of the Si and Fe concentrations, and solidification rate, J. Alloy. Compd. 577 (2013) 103–124.
[35] J. Gan, J. Du, C. Wen, G. Zhang, M. Shi, Z. Yuan, The effect of Fe content on the solidification pathway, microstructure and thermal conductivity of hypoeutectic Al–Si alloys, Int. J. Met. (2022) 1–13.
[36] Y. Liu, S. Kang, The solidification process of Al–Mg–Si alloys, J. Mater. Sci. 32 (1997) 1443–1447.
[37] H. Fang, Q. Tang, Q. Zhang, T. Gu, M. Zhu, Modeling of microstructure and microsegregation formation during solidification of Al-Si-Mg alloys, Int. J. Heat Mass Transf. 133 (2019) 371–381.
[38] X. Ao, H. Xia, J. Liu, Q. He, S. Lin, A numerical study of irregular eutectic in Al-Si alloys under a large undercooling, Comput. Mater. Sci. 186 (2021) 110049.
[39] J. Li, P. Jiang, S. Geng, J. Xiong, Numerical and experimental study on keyhole dynamics and pore formation mechanisms during adjustable-ring-mode laser welding of medium-thick aluminum alloy, Int. J. Heat Mass Transf. 214 (2023) 124443.
[40] L. Huang, X. Hua, D. Wu, L. Fang, Y. Cai, Y. Ye, Effect of magnesium content on keyhole-induced porosity formation and distribution in aluminum alloys laser welding, J. Manuf. Process. 33 (2018) 43–53.
[41] V.B. Biscuola, M.d.A. Martorano, Mechanical blocking mechanism for the columnar to equiaxed transition, Metall. Mater. Trans. A 39 (2008) 2885–2895.
[42] S. Kang, J. Shin, Numerical and experimental study on melt-pool heat transfer and weld characteristics in dual-mode fiber laser welding of aluminum alloy, Opt. Laser Technol. 158 (2023) 108805.
[43] S. Kou, Welding Metallurgy, John Wiley & Sons, New Jersey, USA, 2003.
[44] G. Ma, K. Yue, D. Liu, R. Wang, F. Niu, D. Wu, Cracking susceptibility control of 7075 aluminum alloy in pulsed laser welding with filler strip, Opt. Laser Technol. 152 (2022) 108119.